Geopersia 2023, 13(1): 123-143
DOI: 10.22059/GEOPE.2023.350569.648686

RESEARCH PAPER

Mineral chemistry and petrology of magmatic rocks from NW Takestan (NW Iran)

Ali Asghar Sepahi [1,2,] *, Batool Nemati [1], Abbas Asiabanha [3], Mirmohammad Miri [4], Kiymet Deniz [5]

[1] Department of Geology, Faculty of Science, Bu-Ali Sina University, Hamedan, Iran
[2] Department of Geology, Faculty of Science, Ferdowsi Univesity of Mashshad, Mashhad, Iran
[3] Department of Geology, Faculty of Science, Imam Khomeini International University, Qazvin, Iran
[4] Department of Geology, Faculty of Earth Science, Shahid Chamran University of Ahvaz, Ahvaz, Iran
[5] Department of Geological Engineering, Earth Sciences Application and Research Center (YEBIM), Faculty of Engineering, Ankara University, Turkey

Received: 31 October 2022, Revised: 28 December 2022, Accepted: 06 January 2023

Abstract

In northwest of the Takestan area (NW Iran), as a part of the western Alborz mountain belt, various plutonic (monzodiorite, quartz monzonite, granite, and alkali granite), volcanic (andesite, basalt, basaltic andesite, rhyolite, and dacite) and pyroclastic rocks (tuff, agglomerate, and ignimbrite) are hosted of Eocene age. Electron probe micro analyzing (EPMA) on clinopyroxene, orthopyroxene, biotite, and amphibole show that they are diopside to augite (Mg# = 0.6-0.8), enstatite (Mg# = 0.63-0.68), annite to phlogopite (Fe# = 0.15 - 0.3) and pargasite (Mg# = 0.6 - 0.8), respectively. The plagioclases have different compositions with normal chemical zoning from labradorite (in the basalts, An% = 40 - 60) to andesine (in the monzodiorite, An% = 27 - 50) to oligoclase (in the other rocks, An% = 13 - 38). All minerals are primary magmatic except for the alkali granite biotites that have low Ti contents which indicate that they formed by re-equilibrium with a hydrothermal fluid. Chemical compositions of the clinopyroxene, biotite, and amphibole reveal that they crystallized from calc-alkaline magmas formed by subduction of Neo-Tethys oceanic crust beneath the Iran micro-plate. Geothermometry calculations based on the mineral compositions indicate ca. 880 to 980 °C for the basalts, 800 to 850 °C for the andesite and the dacite, 750 to 820 °C for the monzodiorites and the quartz monzonite, and 520 to 670 °C for the alkali granite. High Al contents of the plagioclases from the quartz monzonite and monzodiorite as well as Fe^{+3} contents of the biotites from the alkali granite show that they formed from oxidized magmas that were suitable for Cu porphyry systems. Propylitic and argillic alteration zones in the area confirm it.

Keywords: Mineral Chemistry, Alkaligranite, Dacite, Basalt, Andesite, Neo-Tethys, Alborz Mountain Belt, Takestan, Eocene.

Introduction

Chemical compositions of igneous minerals provide important information about their parental magma. Temperature, pressure and oxygen fugacity conditions of magma during crystallization can be estimated using mineral chemistries (e.g., Hammarstrom & Zen, 1986; Hollister et al., 1987; Johnson & Rutherford, 1989; Blundy & Holland, 1990; Schmidt, 1992; Holland & Blundy, 1994; Anderson & Smith, 1995). Clinopyroxene, biotite, and amphibole formed from magmas of different tectonic settings can discriminate these conditions by using their cation

---

* Corresponding author e-mail: sepahi@basu.ac.ir

contents, such as Al, Fe, Mg and Ti (e.g. Nisbet & Pearce, 1977; Leterrier et al., 1982; Abdel-Rahman, 1994; Molina et al., 2009). Crystallization depth of calc-alkaline magmas reveals conditions and evolution of magmas in orogenic belts (Rutter et al., 1989).

The Takestan area northwest of Iran and west of Alborz mountain belt (AMB), hosts granitoid bodies including monzodiorite, quartz monzonite, granite, and alkali granite together with some andesite, basalt, basaltic andesite, rhyolite, and dacite, as well as pyroclastic units, such as tuffs, agglomerates, and ignimbritic flows. Whole-rock geochemistry of volcanic rocks in western AMB (Alborz-Azarbayjan magmatic belt) indicate that they are products of fractional crystallization of parental magmas that originated during subduction of the Neo-Tethys oceanic lithosphere beneath the Iran micro-plate during the Tertiary (e.g. Asiabanha et al., 2009; Asiabanha & Foden, 2012; Omrani et al., 2013; Nabatian et al., 2015). According to Asiabanha et al. (2012), volcanic rocks of western AMB are calc-alkaline to shoshonitic and possess geochemical characteristics of continental arcs and back-arc extensional setting. Ashrafi et al. (2019) also reported SiO_2-undersaturated intrusive rocks (foid-bearing monzonite and syenite). Chiu et al. (2013) suggested zircon U-Pb age of 35.8± 0.3 Ma (Late Ecocene) for a basaltic andesite from the Qazvin area. Similar ages of 35 - 37 Ma were reported for the Tarom-Olya pluton (diorite, monzonite, quartzmonzonite and monzogranite) from western AMB (Nabatian et al., 2015). A whole-rock geochemical study (Foudazi et al. 2015) shows that the igneous rocks of NW Takestan are high calc-alkaline formed in a volcanic arc setting.

All the previous studies used whole-rock geochemical data to investigate petrogenesis and tectonic history of magmatic rocks in western AMB. However, they have not been studied using chemistry of the minerals. In this paper, we provide a whole set of EPMA data for olivine, clinopyroxene, orthopyroxene, hornblende, plagioclase, and biotite from magmatic rocks of NW Takestan to compare the results with those of whole-rock geochemistry studies. Moreover, the ore mineralization potential of the intrusive rocks is examined, using biotite and plagioclase compositions.

Geological setting

The study area belongs to the AMB, north of Iran (Fig. 1a). The AMB is a part of the Alpine–Himalayan orogenic belt in western Asia (Stöcklin, 1974) between the Caspian Sea to the north and the Iranian Plateau to the south. It formed during subduction of the Neo-Tethys oceanic lithosphere beneath the Iranian micro-plate and collision of Arabia with Eurasia during the Alpine-Himalayan orogeny (Stöcklin, 1974; Berberian & Berberian, 1981). Zanchi et al. (2006) considered that the AMB as an orogenic belt resulted from Paleo-Tethyan and Neo-Tethyan closures during the Late Triassic. During the Cenozoic, widespread magmatic activities occurred in Iran in relation to subduction of the Neo-Tethys oceanic lithosphere beneath the CIB, especially along the AMB and the Urumieh-Dokhtar magmatic belt (UDMB) (Fig. 1a). These activities produced huge and very extensive deposits of pyroclastic, volcanic rocks, and intrusive masses. The present-day intra-continental deformation associated with the Arabian and Eurasian plate convergence due to opening of the Red Sea, affected the structural evolution of the Alborz belt (Zanchi et al. 2006; Guest et al. 2007; Agard et al., 2011; Madanipour et al. 2013).

The N-S trending Rasht-Takestan Fault divides the AMB into western and eastern segments. The western segment (Alborz-Azarbayjan magmatic belt) consists of andesitic-dacitic lava and tuffs that were intruded by several granitoid bodies of calc-alkaline to alkaline affinity while the eastern segment is composed of alkaline to shoshonitic basic and acidic tuff and lava (e.g. Aghazadeh et al., 2011; Castro et al., 2013; Nabatian et al., 2015). Annells et al. (1975) considered that the igneous rocks of the western Alborz zone (Taleghan and Qazvin regions) formed in three phases. Phase 1 (with Eocene age) is dominated by acidic and andesitic tuffs plus mudstone tuffs, and phases 2 and 3 (with Oligocene age) include basic lavas and andesitic-acidic lavas, respectively. Asiabanha et al. (2009) divided the western Alborz volcanic rocks into three stages: submarine eruptions, surface eruptions, and plutonism. Thickness of lava flows and the ratio of lava flow to the pyroclastic rocks increases to the west (Asiabanha & Foden, 2012).

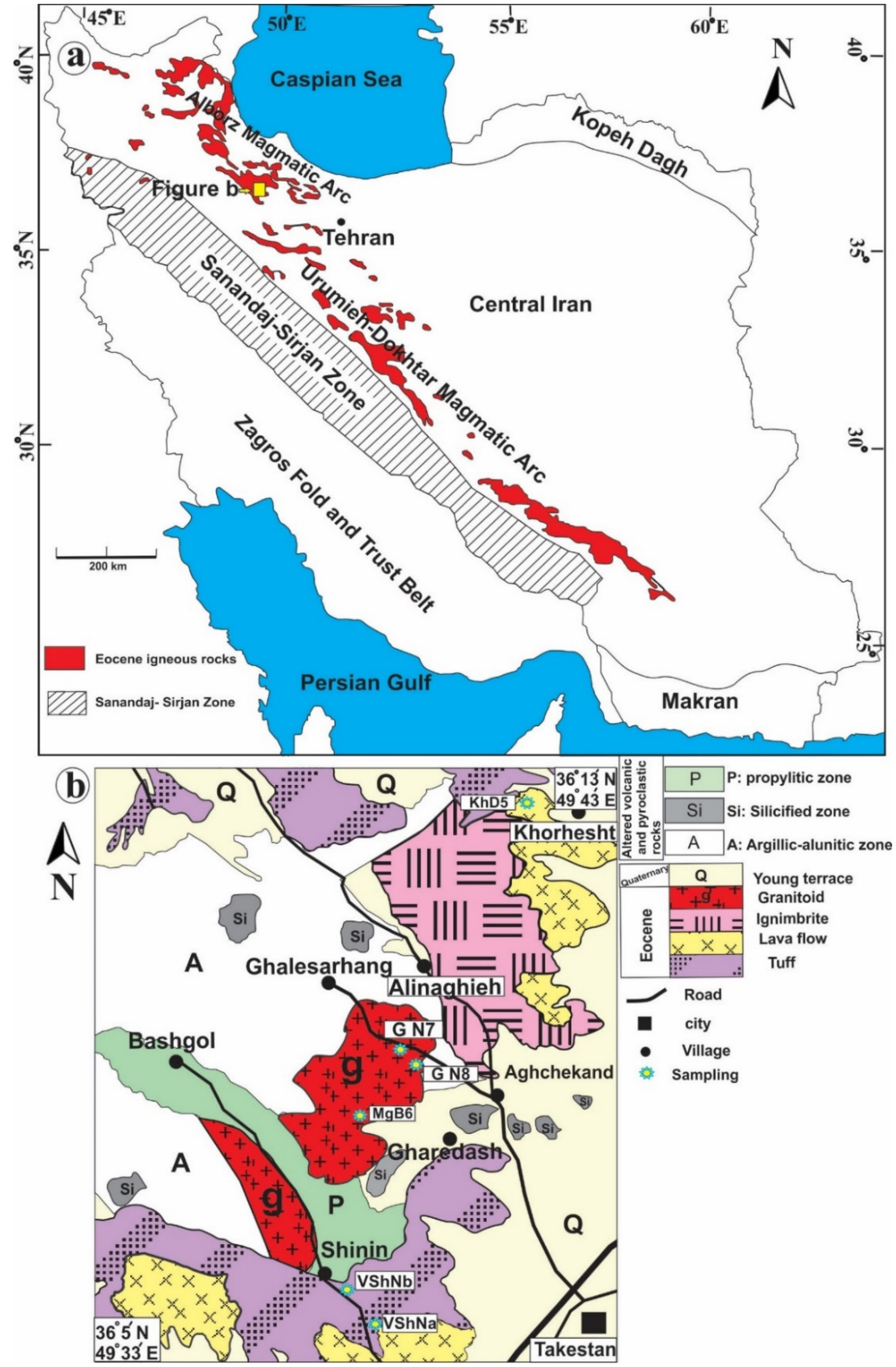

Figure 1. (a) Location of the area, the magmatic arc of Alborz and Urumieh - Dokhtar in the structural map of Iran (modified from Mohajjel and Fergusson, 2014) with a slight change; (b) lithologies of the area in the 1: 100000 map of Takestan (modified from Alai Mahabadi and Fonoudi, 1992) and locations of the samples

There are several reasons for intensive magmatism in the Eocene, including the development of the rift/back arc basin (Amidi et al., 1984; Amidi and Michel, 1985; Kazmin et al., 1986), changes in the subduction angle (Barbarian and Barbarian, 1981; Shahabpour, 2007), and changes in subduction velocity (Takin, 1972; Pazirandeh, 1973; Kazmin et al., 1986). According to Moin-Vaziri (2004), the main cause of the Eocene's massive magmatism in Iran is the breaking of the oceanic crust of Neo-Tethys in the Upper Cretaceous. Verdel et al. (2011) argued that slab roll-back in the Eocene caused extensional regime and asthenosphere upwelling.

The study area, as mentioned above, contains both intrusive and volcanic rocks of Eocene (Alai Mahabadi and Fonoudi, 1992). The phase I pyroclastic rocks, crop out in northern and southern parts of the area in the form of thin and thick layers and in some places masses of large extent and thickness. The phase II lavas overlay phase I tuffs although in a more limited expansion (Fig. 2a). Sub-volcanic dacitic and rhyolitic domes (Figure 2, b) as well as granitoid intrusive bodies (monzodiorite, quartz monzonite, and alkali granite) of the phase III, subsequently or simultaneously intruded the phase I tuffs (Fig. 2c). Alterations are dominant in the area that consist of argillic-alunitic, silicified and propylitic zones (Fig. 1b), indicating possibility of ore mineralization.

The study method

About 120 samples from different volcanic, intrusive, and pyroclastic rocks were collected and studied using a polarizing microscope. Six samples (3 intrusive and 3 volcanic samples) containing suitable minerals were selected for electron microprobe analysis (EPMA).

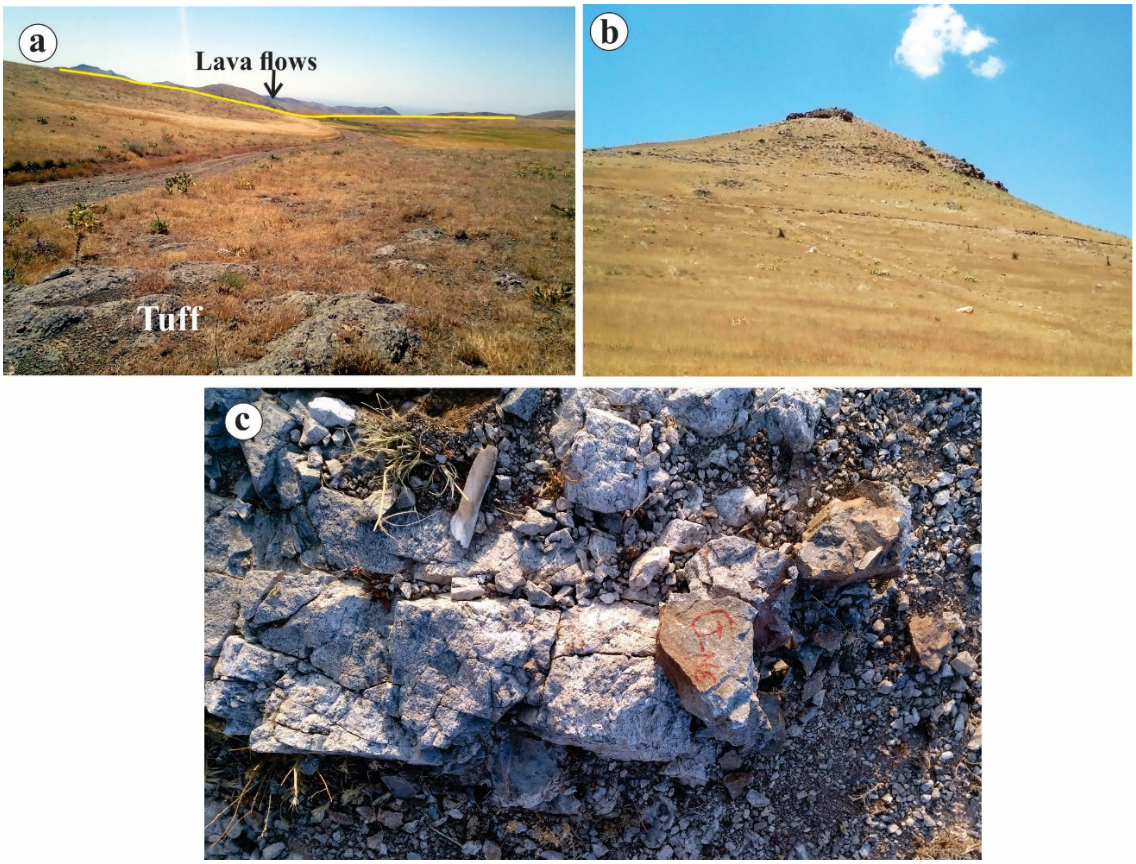

Figure 2. (a) Placement of lava flows on the tuff; (b) Aqcheh Kand dacite dome in the area; (c) the alkali granite rocks in the area

The analyzes were performed in the laboratories of the Department of Geological Engineering and Application and Research of Earth Sciences of Ankara University (YEBİM-Ankara, Turkey) using a JEOL JXA 8230 device under 20 kV voltage and 10 nA beam current, 2 µm spot size and 10 minutes counting time. The matrix effect was corrected using ZAF method. About 200 points were analyzed from olivine, pyroxene, biotite, amphibole, plagioclase, alkali feldspar, titanite, and opaque minerals. Representative analyses are in Table 1 to 4 and the whole set of data is given in the Supplementary (Table 1). Ferric and ferrous iron contents in olivine, pyroxene and biotite were calculated using Droop (1987) and those of the amphibole using Schumacher (2007) methods.

Petrography

Alkali granite

Granular hypidiomorphic is the main texture but granophyric and perthite textures are in some samples (Fig. 3a, b). These rocks generally contain orthoclase (50-40 vol%), quartz (20-30 vol %), plagioclase (<10 vol%), and biotite (<10 vol%) (Fig. 3a, b). The accessory minerals are sphene (titanite), apatite, zircon and opaque minerals. In some samples, in addition to primary titanites and secondary titanites formed due to the alteration of opaque minerals or biotites.

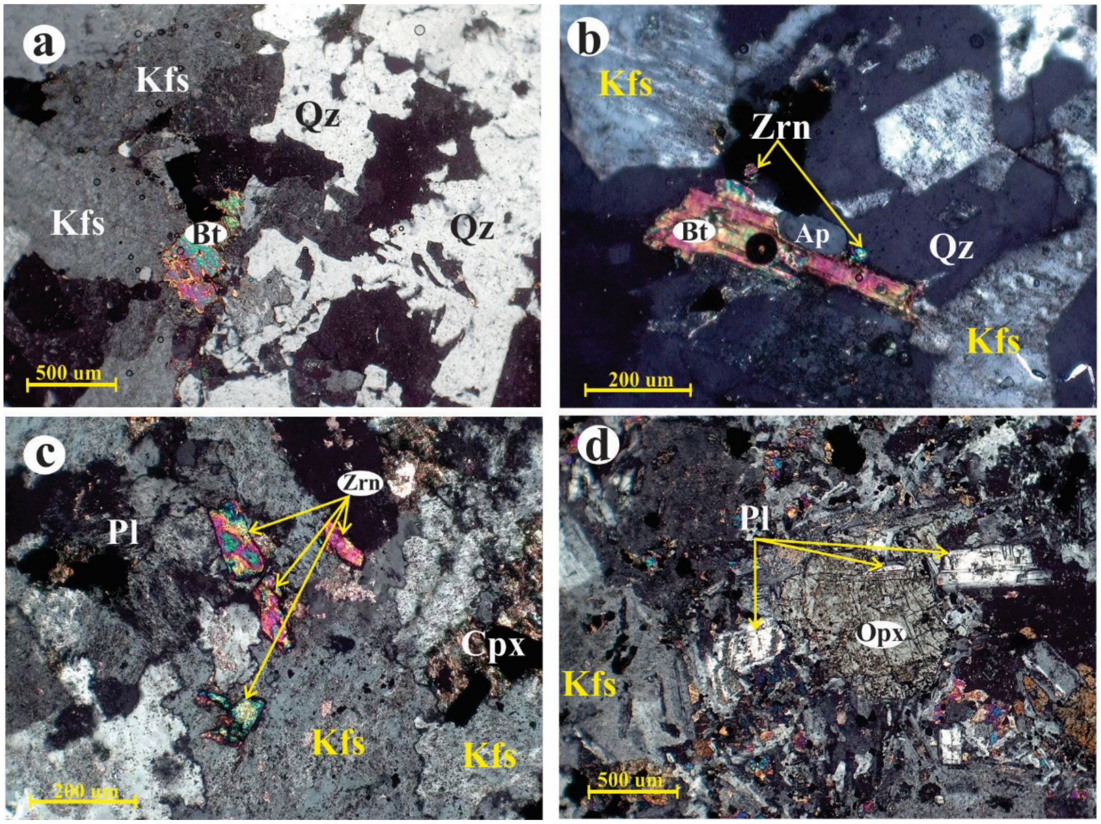

Figure 3. Photomicrographs of intrusive rocks from the area; (a) granular and granophyric textures in the alkali granite (sample MGB6); (b) perthitic orthoclase together with zircon and apatite in the alkali granite (sample MGB6); (c) perthitic orthoclase and plagioclase with suture boundaries in the quartz monzonite. The clinopyroxene is replaced by chlorite and opaque minerals (sample GN7); (d) ophitic and sub-ophitic textures in monzodiorites (sample GN8). All photomicrographs are in crossed polarized light (XPL). Mineral abbreviations are Ap: apatite; Bt: biotite; Cpx: clinopyroxene; Kfs: K-feldspar; Opx: orthopyroxene; Pl: plagioclase; Qz: quartz; Zrn: zircon (Whitney & Evans, 2010)

The granophyric and perthitic texture indicate crystallization under low H_2O pressure conditions at a shallow depth and near the surface (Blatt et al., 2006).

Quartz monzonite

These rocks also have subhedral granular and perthite textures (Fig. 3c-d). The main minerals are plagioclase (50-40 vol%), orthoclase (15-20 vol%), clinopyroxene (25-20 vol%), quartz (5-10 vol%) and minor biotites (> 5 vol%). Zircon, apatite and opaque minerals are the minor minerals with different abundances in the samples. Sericite, chlorite, actinolite, and epidote are the secondary minerals formed by alterations of the feldspars and clinopyroxenes. Suture boundaries of the grains show that the rocks underwent some deformations.

Monzodiorite

The main texture of monzodiorites is subhedral granular. Ophitic and sub-ophitic textures are also present (Fig. 3d). Plagioclase (50-40 vol%), pyroxene (40-30 vol%), orthoclase (15-10 vol%), and quartz (<5 vol%) are the main minerals. Opaque minerals, apatite and zircon are minor minerals. Alteration replaced some of the pyroxenes by chlorite, biotite, actinolite, and opaque minerals. The feldspars also are sericitized. Ophitic and sub-ophitic textures indicate shallow level emplacement of the rocks in the form of a dike.

Dacite

Vitroporphyry is the main texture in these rocks (Fig. 4a). The main phenocrysts are plagioclase, biotite, amphibole, clinopyroxene, and quartz. The minor minerals are apatite and zircon that commonly occur around opaque minerals. The primary biotites and amphiboles are opacified (Fig. 4a) which can be a sign of high oxygen fugacity and water vapor pressure while the minerals were forming and of water loss during magma eruption (Best and Christiansen, 2001). The pyroxenes are mostly replaced by secondary small biotites.

Andesite and trachyandesite

These rocks have vitroporphyric and glomeroporphyric textures with plagioclase, amphibole, and biotite as the phenocrysts (Fig. 4b). The minor minerals are apatite, zircon, and opaque minerals. The plagioclases have been calcified and sericitified to some extent. Opacitic and iddingsitic amphiboles are common.

Basalt and basaltic andesite

The rocks generally show porphyritic, microlitic, trachytic and microlitic porphyritic textures (Fig. 4c). In some samples, vesicular and amygdaloidal textures are present, which are filled with secondary minerals such as calcite. The major phenocrysts include plagioclase and pyroxene. Fine-grained iddingsitic olivines occur in the matrix. In some samples, fine pyroxene crystals surround quartz xenocrysts (ocellar quartz) (Fig. 4d). Vernon (1991) argued that the presence of ocellar quartz is evidence of hybridism (hybridization by magmatic mixing). The rounded and embayed texture plagioclases (Fig. 4e) may support this possibility. The plagioclases commonly show optical zoning with sieve texture in the centers (Fig. 4e). A thin layer of fine clinopyroxene formed around some orthopyroxene phenocrysts indicating possibility of magma mixing or mingling (Fig. 4f). In the altered samples, chlorite, actinolite, and opaque minerals replace the pyroxenes.

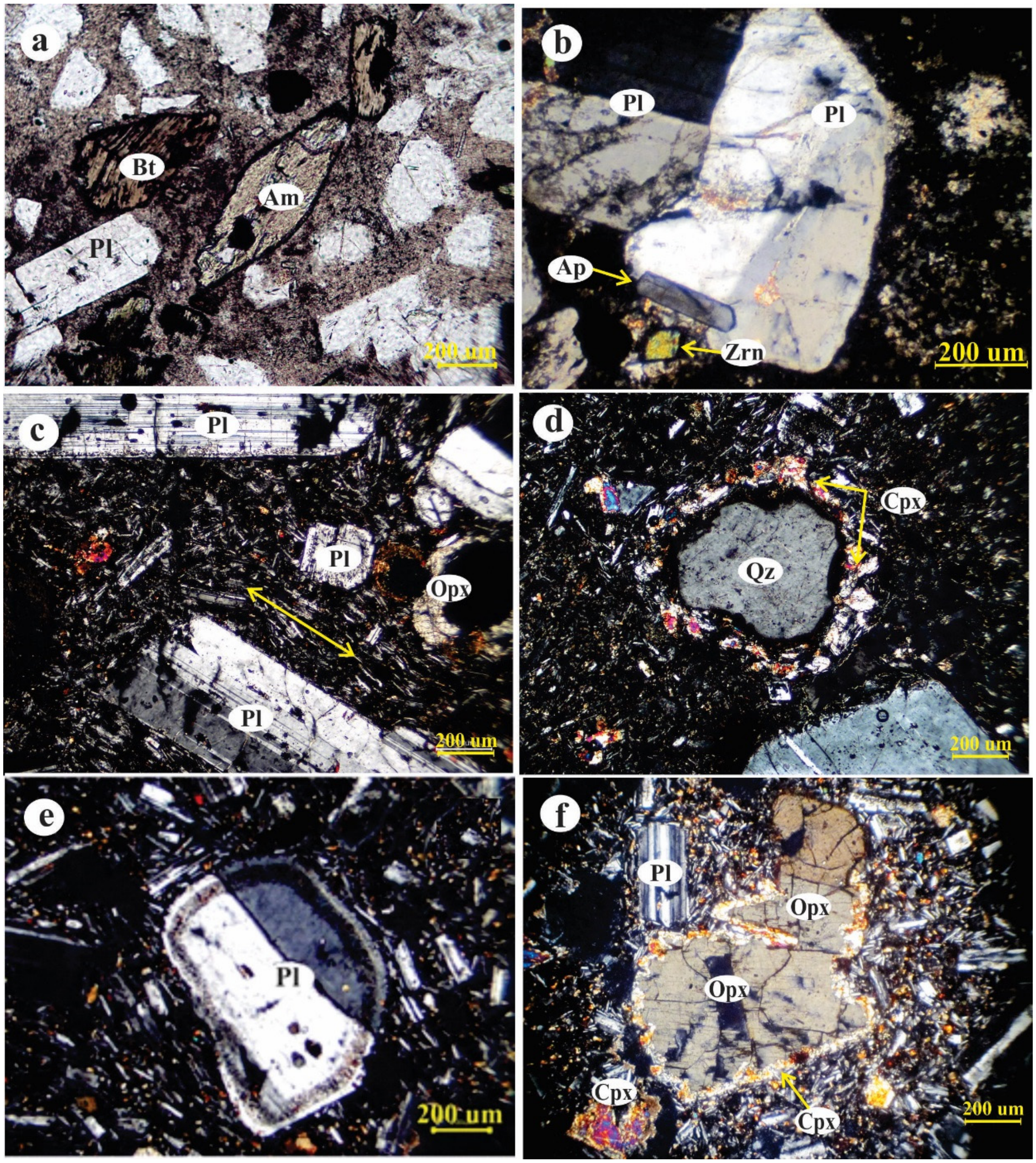

Figure 4. Photomicrographs of volcanic rocks in the NW of Takestan area. (a) vitroporphyric texture and opacitic amphibole and biotite in the dacite (sample KhD5); (b) glomeroporphyric texture in the andesite (sample VShNa); (c) trachytic and porphyritic textures with plagioclase and orthopyroxene phenocrysts in the basaltic andesite (sample VKhN12); (d) ocellar quartz xenocryst in the basaltic andesite (sample VKhN12); (e) sieve textured rounded plagioclase phenocryst in the basalt (sample VShNa); (f) thin layer of fine-grained clinopyroxene around a pyroxene phenocryst in the basalt (sample VShNa). The Fig. a, is in plane polarized light (PPL) and the others are in XPL. Mineral abbreviations as the Fig. 3

Mineral chemistry

Olivine

Olivine is only visible as fine grains in the basalt and basaltic andesite samples. Some olivines from basalts were analyzed in this study (Table 1 and Supplementary Table 1). The olivine forsterite contents range 36.97 to 61.92% that classified it as hortonite to ferrohertonite according to Klein & Hurlbut (1985).

Pyroxene

Except for the alkali granites, all the rocks contain clinopyroxene and the basalts have orthopyroxene. The clinopyroxene have different compositions in the samples. In the basalts, they have low wollastonite contents (Table 2 and Supplementary Table 1) and and lie in the field of augite in the pyroxene classification diagram (Moromito et al., 1988) (Fig. 5a). The other clinopyroxenes contain moderate wollastonite and high enstatite contents that classify them as diopside (Fig. 5a). The orthopyroxenes from the basalts have high Mg/Fe contents and plot in the field of enstatite but near the field of pigonite (Fig. 5a). For comparison of the clinopyroxenes in different rocks, their Al and Mg# [Mg/(Mg+Fe^{+2})] contents are plotted against Si (Fig. 5b and c). The diagrams show that the basalt clinopyroxenes have lower Mg# and Si but higher Al than most of the others, indicating crystallization under different conditions.

Amphibole

Amphiboles are present in andesitic and dacite samples, but they could not be analyzed in the dacite due to high opacification. Structural formulae of the analyzed amphiboles from the andesite were calculated based of 23 Oxygens and normalized to 13 cations except for Ca, Na, and K (13eCNK) ((Table 4 and Supplementary Table 1)). Based on the Ca_B contents (1.7 - 1.8), they are classified as calcic amphiboles (Leake et al., 1997). On the Al + Fe + 2Ti versus Na+Ka classification diagram (Hawthorne et al., 2012), the samples plot in the pargasite field (Fig. 5d).

Biotite

The analyzed biotites are from the alkali granite and andesite samples (Table 4 and Supplementary Table 1). They have relatively different composition (Fig. 5e, F). The biotites from the alkali granite have higher Si and Mg# but lower Al and Ti than those from the andesites. On a $Al^{vi}/(Al^{vi}+Si)$ versus Mg# diagram, the alkali granite biotites plot in the field of phlogopite and the andesite biotites lie in the field of biotite (Fig. 5e). In addition, the andesite biotites are primary formed by crystallization from a magma whereas the alkali granite biotites formed due to re-equilibration with a hydrothermal fluid after they crystallized (Fig. 5f).

Plagioclase and K-feldspar

The Fig. 6a and b diagrams show diversity of the plagioclase compositions in the samples. The anorthite contents range 42 - 60% for the basalts, 19 - 27% for the andesites, 20 - 27% for the dacites, 11 - 36% for the quartz monzonites, 27 - 50 for the monzodiorite and 12 - 39% for the alkali granites (Table 3 and Supplementary Table 1). In addition, the plagioclases mostly show normal chemical zoning. In general, anorthite contents decrease toward the rims, however irregularly in most places (Fig. 6c, d).

The K-feldspars from the alkali granites and quartz monzonites have relatively uniform compositions. They contain high orthoclase contents (> 73%) and lie in the field of sanidine on the feldspar classification diagram (Fig. 6a). There was no significant chemical zoning in them.

Table 1. Representative chemical compositions of the olivines and orthopyroxenes from the basalts

Olivine					Orthopyroxene							
Sample	**VShNb**	**VShNb**	**VShNb**	**VShNb**	**Sample**	**VShNb**	**VShNb**	**VShNb**	**VShNb**	**VShNb**	**VShNb**	**VShNb**
SiO_2	37.50	37.87	36.41	36.29	SiO_2	51.41	52.37	51.41	51.41	50.37	50.54	52.11
TiO_2	0.07	0.03	0.01	0.03	TiO_2	0.37	0.39	0.37	0.37	0.35	0.35	0.44
Al_2O_3	0.18	0.04	0.02	0.02	Al_2O_3	1.27	1.24	1.27	1.27	1.04	1.08	1.36
FeO*	34.09	32.34	35.76	35.79	FeO	22.86	22.36	22.86	22.86	21.93	21.95	22.87
MnO	0.00	0.00	0.00	0.00	MnO	0.00	0.00	0.00	0.00	0.00	0.00	0.00
MgO	27.04	29.81	27.70	27.57	MgO	21.38	21.40	21.38	21.38	22.04	22.22	21.16
CaO	0.37	0.26	0.25	0.25	CaO	2.01	2.03	2.01	2.01	1.87	1.89	2.08
Na_2O	0.05	0.00	0.00	0.00	Na_2O	0.07	0.05	0.07	0.07	0.03	0.03	0.06
K_2O	0.06	0.01	0.00	0.00	K_2O	0.00	0.00	0.00	0.00	0.01	0.00	0.00
Total	99.34	100.36	100.16	99.97	Total	99.37	99.84	99.37	99.37	97.64	98.07	100.10
Si	1.04	1.03	1.01	1.01	Si	1.93	1.96	1.93	1.93	1.92	1.91	1.95
Al	0.01	0.00	0.00	0.00	Ti	0.01	0.01	0.01	0.01	0.01	0.01	0.01
Ti	0.00	0.00	0.00	0.00	Al	0.06	0.05	0.06	0.06	0.05	0.05	0.06
Fe^{+2}	0.79	0.73	0.83	0.83	Fe^{+3}	0.07	0.01	0.07	0.07	0.10	0.11	0.03
Mn	0.00	0.00	0.00	0.00	Fe^{+2}	0.65	0.69	0.65	0.65	0.60	0.59	0.69
Mg	1.11	1.20	1.14	1.14	Mn	0.00	0.00	0.00	0.00	0.00	0.00	0.00
Ca	0.01	0.01	0.01	0.01	Mg	1.20	1.19	1.20	1.20	1.25	1.25	1.18
Na	0.00	0.00	0.00	0.00	Ca	0.08	0.08	0.08	0.08	0.08	0.08	0.08
Te	0.00	0.00	0.00	0.00	Na	0.01	0.00	0.01	0.01	0.00	0.00	0.00
Fo	58.24	61.92	57.79	57.64	K	0.00	0.00	0.00	0.00	0.00	0.00	0.00
Fa	41.19	37.69	41.85	41.98	Wo	4.19	4.14	4.19	3.92	3.97	4.00	4.27
Mg#	0.59	0.62	0.58	0.58	En	62.01	60.82	62.01	65.48	65.05	65.36	60.39
					Fs	33.81	35.04	33.81	30.60	30.98	30.65	35.33
					Mg#	0.65	0.63	0.65	0.65	0.68	0.68	0.63

Table 2. Representative chemical compositions of the clinopyroxenes

Rock	**Quartz monzonite**				**Basalt**					**Monzodiorite**				**Dacite**			
Sample	**GN7**	**GN7**	**GN7**	**GN7**	**VShNb**	**VShNb**	**VShNb**	**VShNb**	**VShNb**	**GN8**	**GN8**	**GN8**	**GN8**	**KhD**	**KhD**	**KhD**	**KhD**
SiO_2	50.98	52.41	53.04	52.02	51.41	52.37	51.41	51.41	50.37	52.77	52.02	52.42	52.61	52.24	52.85	52.66	50.98
TiO_2	0.17	0.21	0.08	0.05	0.37	0.39	0.37	0.37	0.35	0.23	0.05	0.05	0.06	0.13	0.18	0.18	0.17
Al_2O_3	0.74	0.58	0.34	0.30	1.27	1.24	1.27	1.27	1.04	0.60	0.30	0.28	0.31	0.78	1.07	0.75	0.74
FeO*	9.27	9.44	9.51	8.19	22.86	22.36	22.86	22.86	21.93	8.67	8.19	6.46	6.26	10.42	9.65	9.52	9.27
MnO	0.00	0.00	0.00	0.00	0.00	0.00	0.00	0.00	0.00	0.00	0.00	0.00	0.00	0.00	0.00	0.00	0.00
MgO	13.92	13.80	14.42	13.90	21.38	21.40	21.38	21.38	22.04	14.11	13.90	14.69	14.78	12.96	14.19	14.17	13.92
CaO	21.27	21.42	22.35	22.68	2.01	2.03	2.01	2.01	1.87	21.74	22.68	23.20	23.41	21.42	21.48	20.94	21.27
Na_2O	0.43	0.51	0.32	0.37	0.07	0.05	0.07	0.07	0.03	0.47	0.37	0.23	0.26	0.53	0.38	0.45	0.43
K_2O	0.03	0.02	0.02	0.00	0.00	0.00	0.00	0.00	0.01	0.00	0.00	0.01	0.00	0.01	0.00	0.00	0.03
Total	96.81	98.37	100.08	97.52	99.37	99.84	99.37	99.37	97.64	98.60	97.52	97.35	97.68	98.48	99.79	98.68	96.81
Si	1.96	1.98	1.97	1.98	1.93	1.96	1.93	1.93	1.92	1.99	1.98	1.99	1.99	1.99	1.97	1.99	1.96
Ti	0.00	0.01	0.00	0.00	0.01	0.01	0.01	0.01	0.01	0.01	0.00	0.00	0.00	0.00	0.01	0.01	0.01
Al	0.03	0.03	0.02	0.01	0.06	0.05	0.06	0.06	0.05	0.03	0.01	0.01	0.01	0.04	0.05	0.03	0.03
Fe^{+3}	0.07	0.03	0.06	0.05	0.07	0.01	0.07	0.07	0.10	0.02	0.05	0.02	0.03	0.03	0.03	0.02	0.07
Fe^{+2}	0.22	0.27	0.24	0.21	0.65	0.69	0.65	0.65	0.60	0.25	0.21	0.18	0.17	0.30	0.27	0.28	0.23
Mn	0.00	0.00	0.00	0.00	0.00	0.00	0.00	0.00	0.00	0.00	0.00	0.00	0.00	0.00	0.00	0.00	0.00
Mg	0.80	0.78	0.80	0.79	1.20	1.19	1.20	1.20	1.25	0.79	0.79	0.83	0.83	0.73	0.79	0.80	0.80
Ca	0.88	0.87	0.89	0.93	0.08	0.08	0.08	0.08	0.08	0.88	0.93	0.94	0.95	0.87	0.86	0.85	0.88
Na	0.03	0.04	0.02	0.03	0.01	0.00	0.01	0.01	0.00	0.03	0.03	0.02	0.02	0.04	0.03	0.03	0.03
K	0.00	0.00	0.00	0.00	0.00	0.00	0.00	0.00	0.00	0.00	0.00	0.00	0.00	0.00	0.00	0.00	0.00
Wo	45.39	46.22	48.05	47.30	4.19	4.14	4.19	3.92	3.97	45.61	48.05	48.24	48.56	45.68	44.68	43.94	46.15
En	40.69	41.49	40.98	40.66	62.01	60.82	62.01	65.48	65.05	41.19	40.98	42.48	42.64	38.44	41.06	41.39	42.01
Fs	13.91	12.30	10.97	12.05	33.81	35.04	33.81	30.60	30.98	13.20	10.97	9.27	8.81	15.89	14.26	14.67	11.85
Mg#	0.78	0.74	0.77	0.79	0.65	0.63	0.65	0.65	0.68	0.76	0.79	0.82	0.83	0.71	0.74	0.74	0.78

Table 3. Representative chemical compositions of the plagioclases and K-feldspars. C= core, in= intermediate, r: rim

Rock	**Basalt**			**Abdesite**			**Dacite**		
sample	**VShNb**	**VShNb**	**VShNb**	**VShNa**	**VShNa**	**VShNa**	**KhD5**	**KhD5**	**KhD5**
Poistion	**c**	**in**	**r**	**c**	**in**	**r**	**c**	**in**	**r**
SiO_2	54.69	56.77	56.88	58.51	61.06	62.50	59.09	60.64	60.40
TiO_2	0.11	0.06	0.07	0.01	0.01	0.01	0.00	0.00	0.00
Al_2O_3	30.65	28.33	28.08	26.91	24.68	23.41	25.73	24.96	24.60
FeO*	1.05	0.73	0.69	0.31	0.36	0.59	0.28	0.27	0.32
MgO	0.07	0.06	0.08	0.02	0.01	0.45	0.01	0.01	0.00
CaO	9.38	7.68	7.82	6.87	4.89	3.60	5.30	4.62	4.53
Na_2O	2.87	5.35	5.42	6.63	8.05	8.92	7.73	8.14	8.04
K_2O	0.84	0.77	0.74	0.46	0.81	0.54	0.99	1.03	1.29
Total	99.65	99.75	99.78	99.71	99.86	100.01	99.13	99.65	99.18
Si	2.52	2.57	2.57	2.61	2.72	2.77	2.65	2.70	2.70
Ti	0.00	0.00	0.00	0.00	0.00	0.00	0.00	0.00	0.00
Al	1.66	1.51	1.50	1.42	1.29	1.22	1.36	1.31	1.30
Fe^{+3}	0.04	0.03	0.03	0.01	0.01	0.02	0.01	0.01	0.01
Mn	0.00	0.00	0.00	0.00	0.00	0.00	0.00	0.00	0.00
Mg	0.01	0.00	0.01	0.00	0.00	0.03	0.00	0.00	0.00
Ca	0.46	0.37	0.38	0.33	0.23	0.17	0.25	0.22	0.22
Na	0.26	0.47	0.48	0.57	0.69	0.76	0.67	0.70	0.70
K	0.05	0.04	0.04	0.06	0.05	0.03	0.06	0.06	0.07
An	60.23	42.04	42.28	34.22	23.93	17.66	25.89	22.45	21.98
Ab	33.39	52.97	52.99	59.84	71.33	79.23	68.34	71.59	70.57
Or	6.38	4.99	4.74	5.94	4.74	3.12	5.77	5.95	7.45

Table 3. Continued

Rock	**Quratzmonzonite**			**Monzodiorite**			**Alkali granite**		
sample	**GN7**	**GN7**	**GN7**	**GN8**	**GN8**	**GN8**	**MGB6**	**MGB6**	**MGB6**
position	**c**	**in**	**r**	**c**	**in**	**r**	**c**	**in**	**r**
SiO_2	60.23	63.19	63.94	55.93	60.35	60.26	56.79	59.42	60.54
TiO_2	0.07	0.04	0.01	0.01	0.02	0.02	0.08	0.04	0.03
Al_2O_3	25.41	22.47	22.13	29.71	25.57	25.43	28.55	26.88	25.09
FeO*	0.33	0.30	0.82	0.41	0.30	0.32	0.42	0.38	0.40
MgO	0.02	0.02	0.89	0.01	0.01	0.03	0.00	0.02	0.02
CaO	6.28	2.86	2.31	8.64	5.48	5.29	7.54	6.26	4.56
Na_2O	7.15	10.22	9.79	5.22	7.84	8.07	6.20	7.19	8.39
K_2O	0.32	0.37	0.26	0.17	0.29	0.33	0.25	0.39	0.78
Total	99.80	99.47	100.15	100.11	99.85	99.76	99.84	100.57	99.81
Si	2.70	2.79	2.81	2.52	2.69	2.68	2.55	2.64	2.69
Ti	0.00	0.00	0.00	0.00	0.00	0.00	0.00	0.00	0.00
Al	1.34	1.17	1.15	1.58	1.34	1.33	1.51	1.41	1.31
Fe^{+3}	0.01	0.01	0.03	0.02	0.01	0.01	0.02	0.01	0.02
Mn	0.00	0.00	0.00	0.00	0.00	0.00	0.00	0.00	0.00
Mg	0.00	0.00	0.06	0.00	0.00	0.00	0.00	0.00	0.00
Ca	0.30	0.14	0.11	0.42	0.26	0.25	0.36	0.30	0.22
Na	0.62	0.87	0.83	0.46	0.68	0.70	0.54	0.62	0.72
K	0.02	0.02	0.01	0.01	0.02	0.02	0.01	0.02	0.04
An	32.06	13.11	11.38	47.23	27.38	26.08	39.54	31.74	22.07
Ab	66.01	84.88	87.12	51.66	70.87	71.98	58.89	65.90	73.42
Or	1.93	2.01	1.50	1.11	1.75	1.94	1.56	2.36	4.51

Table 4. Representative chemical compositions of the amphiboles and biotites

Amphibole						**Biotite**								
Type	**Andesite**					**Type**	**Alkaline granite**				**Andesite**			
Sample	**VShNa**	**VShNa-**	**VShNa-**	**VShNa-**	**VShNa**	**Sample**	**MGB6**	**MGB6**	**MGB6**	**MGB6**	**VShNa**	**VShNa**	**VShNa**	**VShNa**
SiO_2	41.31	43.97	42.12	44.34	41.16	**SiO_2**	40.06	40.70	40.42	40.35	36.91	36.57	35.73	37.89
TiO_2	2.45	1.86	2.48	1.79	2.36	**TiO_2**	1.12	1.37	1.37	1.42	5.07	4.81	4.62	4.82
Al_2O_3	10.26	7.17	8.78	7.26	10.91	**Al_2O_3**	11.03	10.41	10.42	10.53	13.14	13.75	13.88	12.38
FeO*	13.67	14.22	13.5	13.27	12.51	**FeO**	15.22	14.20	14.05	13.80	13.11	15.44	16.64	15.88
MnO	0	0	0	0	0	**MnO**	0.00	0.00	0.00	0.00	0.00	0.00	0.00	0.00
MgO	13.57	13.93	13.72	14.25	14.11	**MgO**	17.30	16.93	17.16	17.11	15.71	14.62	14.63	14.03
CaO	10.95	11.25	10.99	11.28	11.13	**CaO**	0.12	0.03	0.03	0.07	0.03	0.03	0.05	0.05
Na_2O	2.64	2.04	2.38	2.1	2.63	**Na_2O**	0.28	0.42	0.35	0.28	0.56	0.64	0.66	0.65
K_2O	0.71	0.78	0.69	0.77	0.6	**K_2O**	8.34	10.10	10.17	10.18	9.86	9.62	9.35	9.23
Total	95.55	95.22	94.66	95.06	95.39	**Total**	93.48	94.17	93.96	93.74	94.41	95.48	95.56	94.94
Si	6.18	6.52	6.36	6.66	6.13	**Si**	2.97	3.04	3.03	3.03	2.84	2.81	2.75	2.90
Al^{iv}	1.81	1.43	1.56	1.28	1.87	**Al**	0.72	0.63	0.65	0.67	1.07	1.09	1.14	0.94
Al^{vi}	0.00	0.00	0.00	0.00	0.04	**Fe^{+3}**	0.31	0.32	0.32	0.31	0.09	0.10	0.11	0.16
Ti	0.28	0.21	0.28	0.20	0.26	**Sum**	4.00	4.00	4.00	4.00	4.00	4.00	4.00	4.00
Cr	0.00	0.00	0.00	0.00	0.00	**Al**	0.25	0.29	0.27	0.26	0.12	0.15	0.12	0.18
Fe^{+3}	0.87	0.81	0.76	0.61	0.87	**Mg**	1.88	1.87	1.90	1.89	1.79	1.65	1.66	1.58
Fe^{+2}	0.84	0.96	0.94	1.06	0.69	**Fe^{+2}**	0.44	0.50	0.50	0.51	0.66	0.76	0.79	0.73
Mn	0.00	0.00	0.00	0.00	0.00	**Fe^{+3}**	0.19	0.06	0.06	0.05	0.09	0.13	0.17	0.13
Mg	3.03	3.08	3.09	3.19	3.13	**Ti**	0.07	0.09	0.09	0.09	0.29	0.27	0.26	0.28
Ca	1.75	1.79	1.78	1.81	1.78	**Sum**	2.83	2.81	2.82	2.81	2.95	2.97	3.00	2.90
Na	0.77	0.59	0.70	0.61	0.76	**K**	0.82	0.96	0.96	0.97	0.95	0.93	0.91	0.90
K	0.14	0.15	0.13	0.15	0.11	**Na**	0.04	0.06	0.05	0.04	0.08	0.10	0.10	0.10
Mg#	0.78	0.76	0.77	0.75	0.82	**Fe#**	0.19	0.21	0.21	0.21	0.27	0.31	0.32	0.32

Opaque minerals

Opaque minerals present in all samples in the area. They are ilmenite in the quartz monzonite, titanomagnetite in the basalts and magnetite in the other samples (Supplementary Table 1).

Discussion

Geothermobarometry

With respect to mineral contents of the rocks, several methods were used for geothermobarometry calculations as follows.

Geothermometry of clinopyroxene

Previous studies show a general trend of increasing Al and Na content in pyroxene with increasing pressure. France et al. (2010) proposed a geothermometers based on aluminum concentration of clinopyroxene. On the basis of this method, the crystallization temperature of clinopyroxene in the rocks are 884 to 983 °C for the basalts, 810 to 841 °C for the dacites, 799 to 836 °C for the andesites, 760 to 821 ° C for the monzodiorites and 759 to 793 ° C for the quartz monzonites (Table 1).

Two feldspar geothermometry

Geothremometer based on compositions of two co-existing feldspars using calibration of

Putirka (2008) was applied for the alkali granite and quartz-monzonite samples. The calculations produced ca. 525 to 670 °C for the alkali granites.

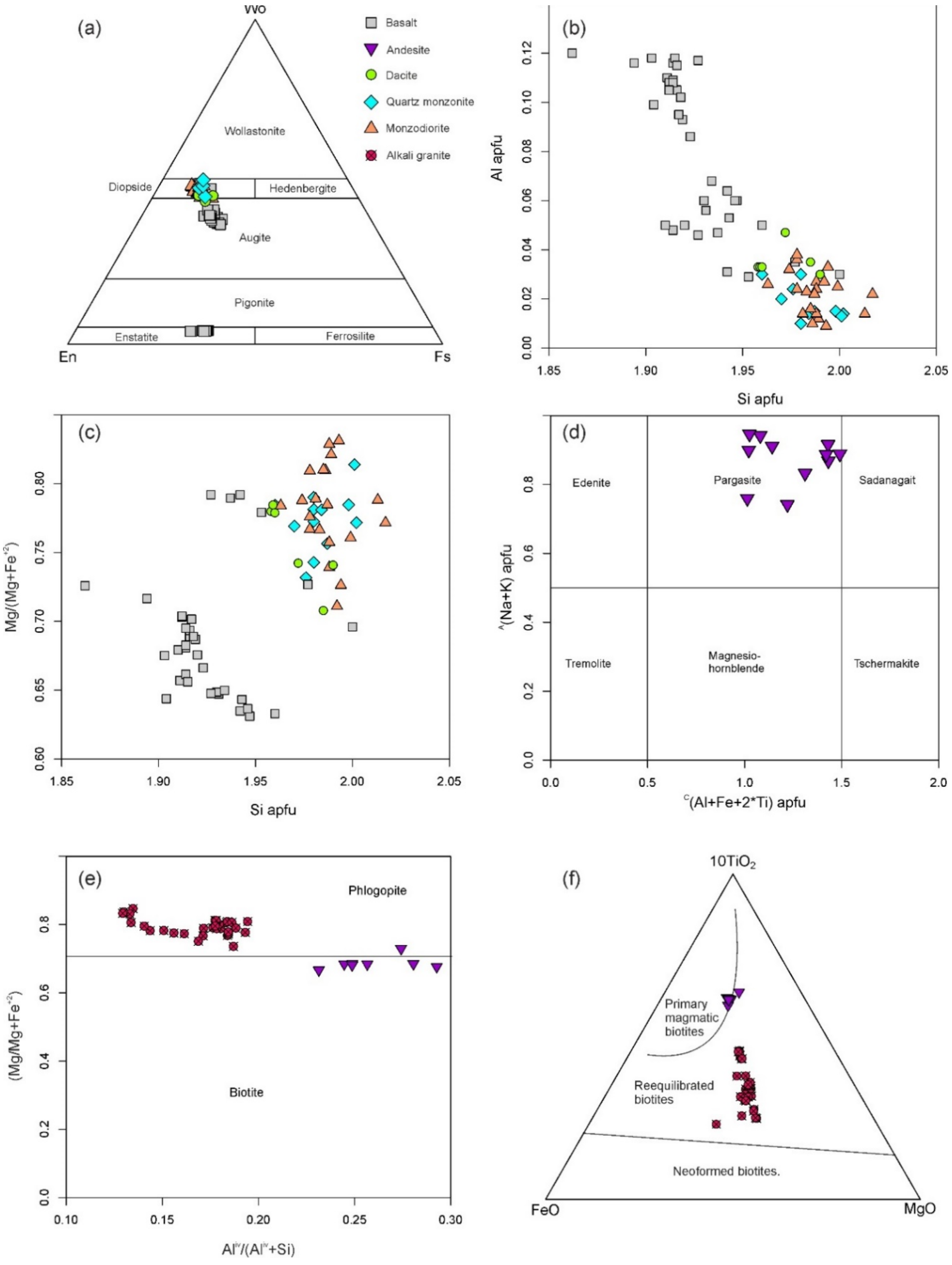

Figure 5. (a) En-Wo-Fe classification diagram (Moromito et al., 1988) for the clinopyroxnenes; (b and c) Si–Al and Si-Mg# diagrams for comparison of the clinopyroxene chemical compoistions from the studied rocks; (d) Al + Fe + 2Ti versus Na+Ka classification diagram (Hawthorne et al., 2012) for the andesite amphiboles; (e) $Al^{vi}/(Al^{vi}+Si)$ versus Mg# diagram classification (Deer et al., 1991) (f) the TiO_2 – FeO – MgO ternary diagram (Nachite et al., 2005) for the biotites

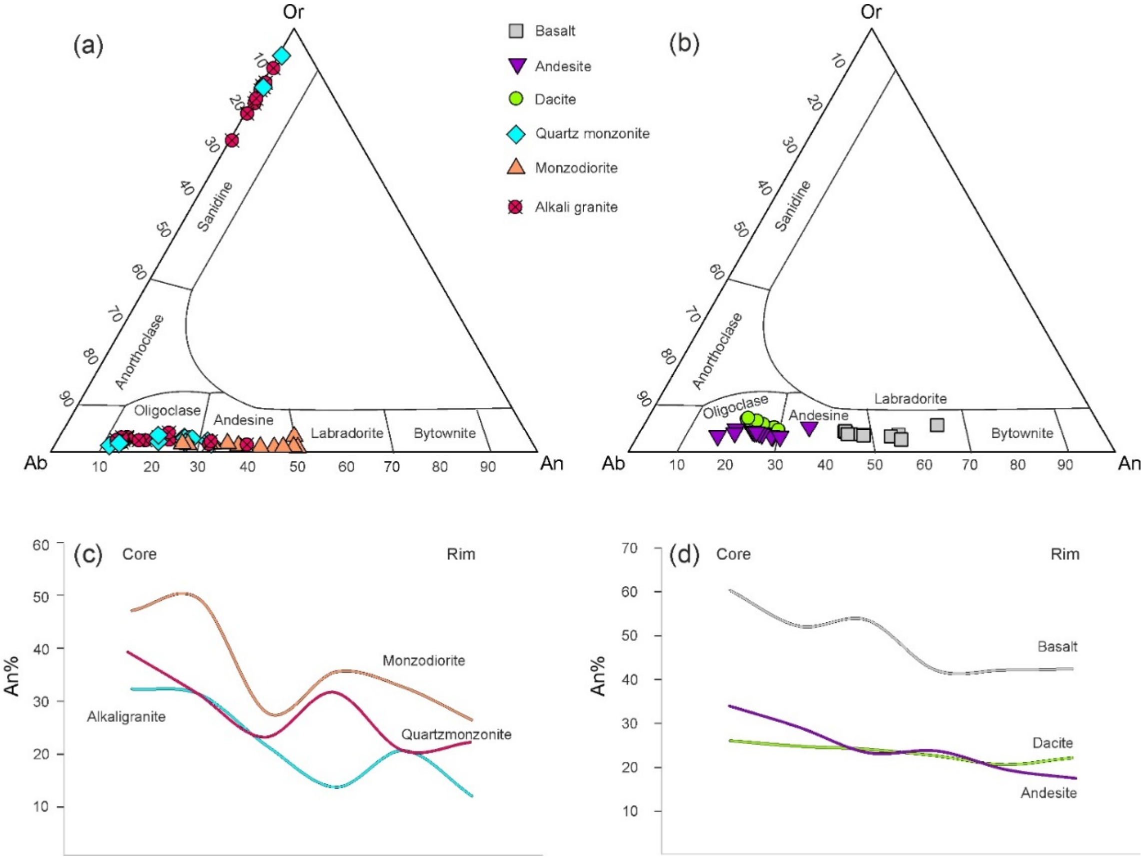

Figure 6. (a) and (b) composition of the feldspars on the Ab-Or-An ternary classification diagram (Deer et al. 1991); (c) and (d) variation of the plagioclase anorthite contents along core to rim chemical profiles

Amphibole and plagioclase geothermobarometry

The hornblende - plagioclase thermometer (Holland & Blundy, 1994) equation for reaction edenite + albite = richterite + anorthite was applied for the andesite samples that lacked quartz in the rock and produced temperatures that range 730 to 800 °C. Compositions of the plagioclase rims were used for the calculations.

Temperatures were determined by using the calculation Al in hornblende barometer based on Anderson and Smith (1995) calibration. The results show that the amphiboles crystallized at ca. 2.8 - 4.2 kbar representing 9 to 13km depth.

Magmatic series

The pyroxene composition depends on the host magma nature (Manoli and Molin 1988; Bindi et al. 1999; Avanzinelli et al. 2004; Zhu and Ogasawara 2004). Therefore, it is proper to investigate the origin and evolution of the host magma, the magmatic series, the physico-chemical conditions, and the tectono-magmatic setting of the host magma (Le Bas 1962; Leterrier et al. 1982; Moromito et al. 1988; Beccaluva et al. 1989; Bindi et al. 1999; Avanzinelli et al. 2004). The clinopyroxenes contain high SiO_2 (> 48 wt%) and relatively low Al_2O_3 (< 2.6 wt%) that resemble clinopyroxenes from the subalkaline magmas (Nisbet and Pearce, 1977) (Fig. 7a). The Al_2O_3 versus TiO_2 diagram (Le Bas et al., 1962) also shows that they crystallized from calc-alkaline magmas (Fig. 7b).

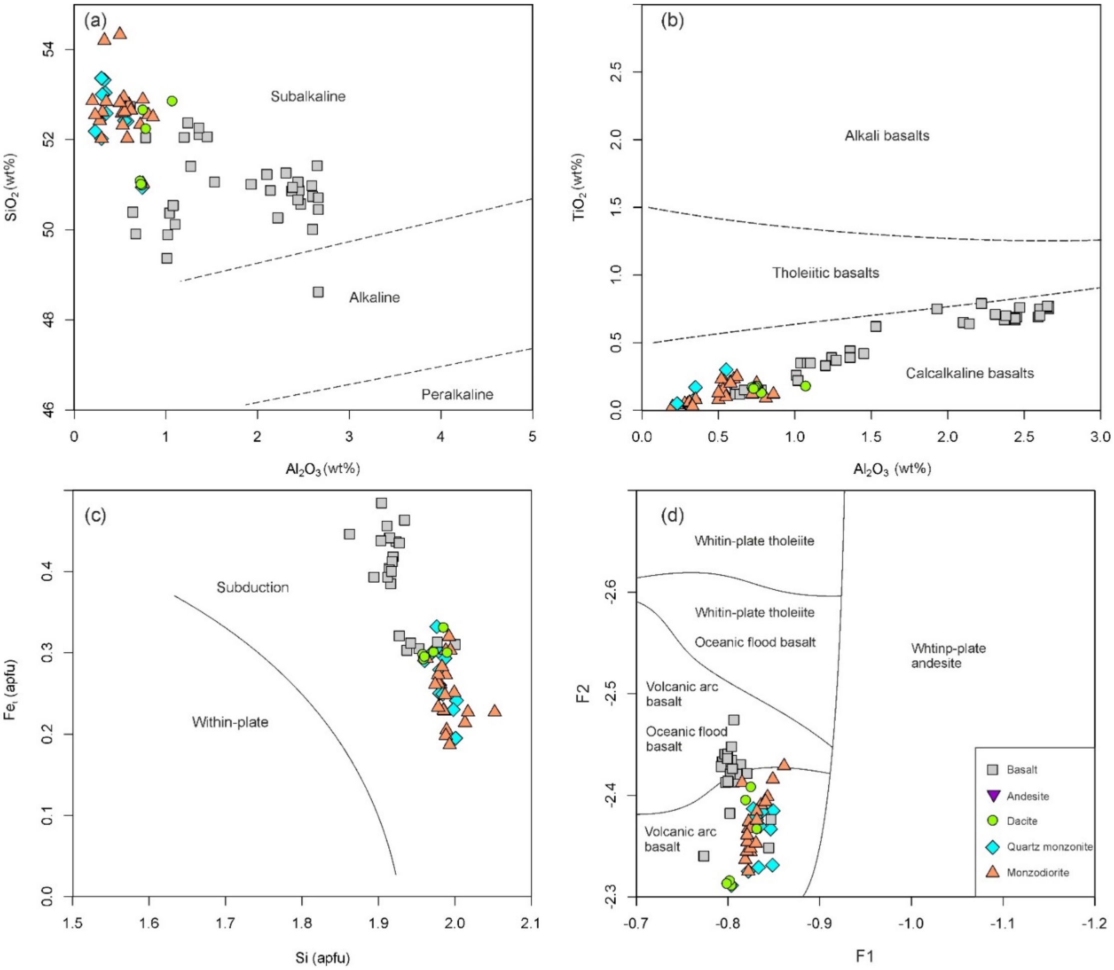

Figure 7. (a) Al_2O_3 versus SiO_2 (Nisbet and Pearce, 1977) and (b) Al_2O_3 versus TiO_2 (Le Bas et al., 1962) magma series discriminating diagrams for the clinopyroxenes; (c) Si versus Fe (Aparicio, 2010) and (d) F1-F2 (Nisbet and Pearce, 1977) tectonic discriminating diagrams for the clinopyroxenes. See the text for F1 and F1 parameters

The amphibole compositions also reflect compositions of their parent magma (e.g. Molina et al., 2009). Compositions of amphiboles from the andesites on Al^{vi} versus K^A and SiO_2 versus TiO_2 discrimination diagrams (Ridolfi et al., 2009; Ridolfi and Renzulli, 2012) are shown in Fig. 8c, d. On the basis of FeO, MgO, and Al_2O_3 contents in biotites in igneous rocks, Abdel-Rahman (1994) suggested some magma series and tectonic and discrimination diagrams. Chemical compositions of biotites from the andesite and alkali granites confirm association with calc-alkaline magma series (Fig. 8a, b).

Tectonic setting

To determine tectonic setting of the rocks we used some diagrams based on chemical compositions of clinopyroxene and biotite. The clinopyroxenes plot in the field of subduction related magmatic rocks on a Si versus Fe diagram (Fig. 7c). Nisbet and Pearce (1977) proposed two complex parameters (F1 and F2) to determine tectonic setting of magmatic rocks using the composition of clinopyroxenes. The $F1 = -0.012\times SiO_2-0.0807\times TiO_2+0.0026\times Al_2O_3-0.0012\times FeO-0.0026\times MnO+0.0087\times MgO-0.0128\times CaO-0.0419\times Na_2O$ and $F2 = -0.0469\times SiO_2-0.0818\times TiO_2-0.0212\times Al_2O_3-0.0041\times FeO-0.1435\times MnO-0.0029\times MgO+0.0085\times CaO+0.0160\times Na_2O$.

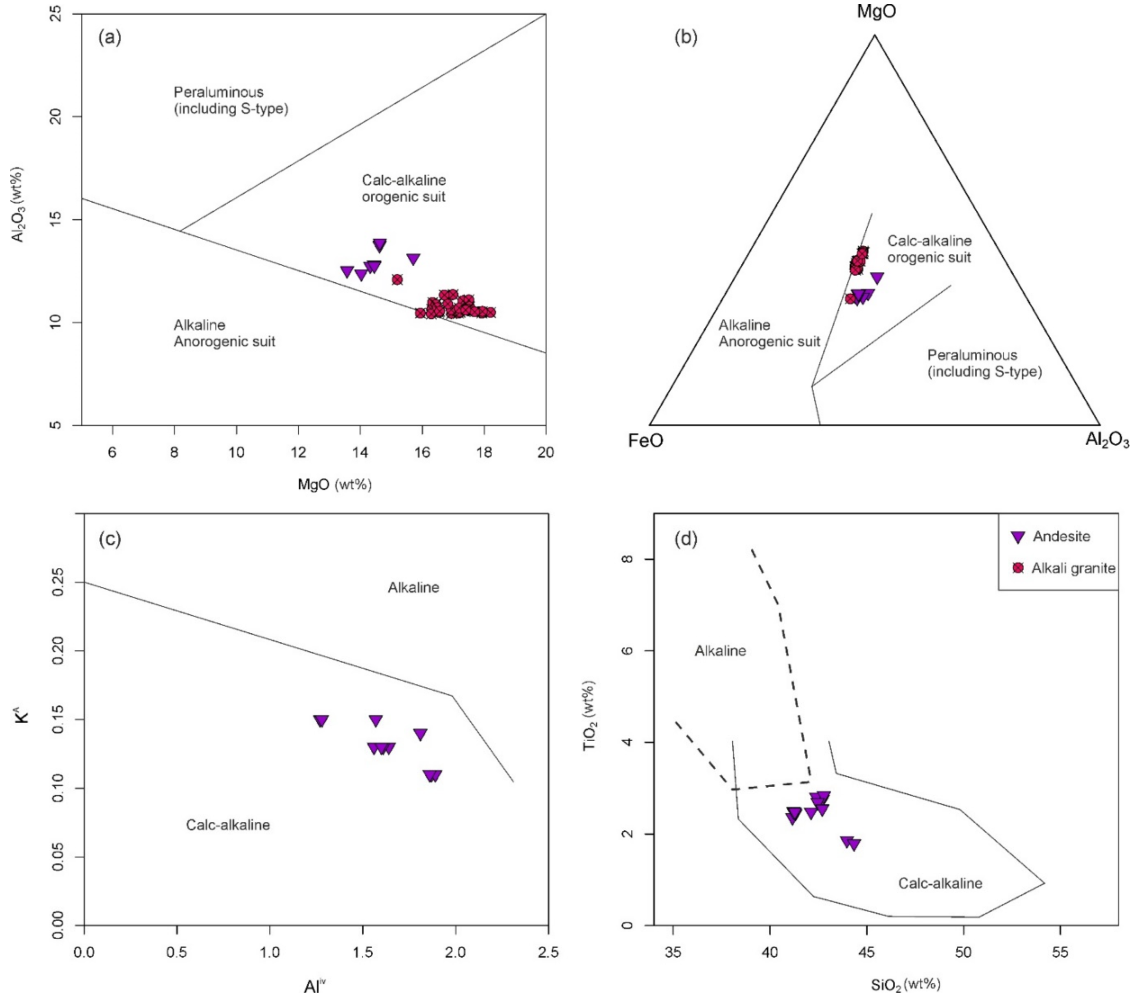

Figure 8. (a and b) MgO versus Al_2O_3 and FeO-MgO-Al_2O_3 diagrams to discriminate magma series and tectonic setting using biotite geochemistry (Abdel-Rahman, 1994); (c) Al^{vi} versus K^A diagram for the (Ridolfi et al., 2009) and (d) SiO_2 versus TiO_2 (Ridolfi and Renzulli, 2012) discrimination diagrams for the andesite amphiboles

The F1 and F2 parameters for the samples range -0.86 to 0.48 and -2.74 to -2.24, respectively. According to these values, the clinopyroxenes lie in the field of volcanic arc on the F1-F2 diagram (Fig. 7d). In addition, as mentioned above, the biotites show affinities with subduction related calc-alkaline magmas (Fig. 8c, d).

Ore mineralization potential

Regarding occurrence of argillic-alunitic, propylitic and silicification alteration zones in the area (Alai Mahabadi and Fonoudi, 1992) and also Cu and Au mineralization south of the Takestan area (Yousefi et al., 2017), we investigated the fertility of the plutonic rocks through chemical compositions of their plagioclases and biotites. Recent studies have indicated that in the porphyry copper systems, plagioclases from the mineralized intrusions might have higher alumina contents relative to the barren ones (e.g., Williamson et al. 2016; Richards, 2016; Zarasvandi et al. 2018; Rezaei and Zarasvandi, 2022). Williamson et al. (2016; 2018) argued that the low average Al contents in plagioclase is most probably due to low PH_2O of melts. The Al/(Ca+Na+K) versus anorthite contents of plagioclase diagram was successful in the discrimination of barren and mineralized intrusions in UDMB (e.g. Zarasvandi et al., 2018;

2020; Rezaei and Zarasvandi, 2022). Compositions of the plagioclases from the quartz monzonite, monzodiorite and alkali granites are plotted on the Al/(Ca+Na+K) versus anorthite contents diagram in Fig. 9a. The Al/(Ca+Na+K) ratios range 1.1 to 1.9 and mostly plot in the field of fertile intrusions. Although, some alkali granite plagioclases plot in the barren intrusion field, they are still in the range of the UDMB porphyry system. Rezaei and Zarasvandi (2022) suggest that the plagioclases that plot above 1:1 ratio line (Fig. 9b) crystallized in an oxidized condition (close to the magnetite–hematite oxygen buffer) that is a common feature for Cu ± Mo porphyry systems (Zarasvandi et al., 2018).

Chemistry of biotite is useful to study hydrothermal evolution (Barrière and Cotten 1979; Van Lichtervelde et al. 2008). The Fe^{3+}/Fe^{2+} of biotite is applicable to study oxygen fugacity of the host magma (e.g. Wones and Eugster, 1965; Danyushevsky and Sobolev 1996; Li et al. 2017). In addition, biotite chemistry has been used to study ore mineralization in many Cu and Cu-Mo-Au porphyry deposits (e.g. Selby and Nesbitt 2000; Boomeri et al. 2010; Siahcheshm et al. 2012; Afshooni et al. 2013; Tang et al. 2019). The biotites formed by re-equilibration of primary biotites (Fig. 5f) with an exsolved magmatic (hydrothermal) fluids that is common in a potassic alteration zone of porphyry systems (e.g., Boomeri et al., 2009; Zarasvandi et al., 2018).

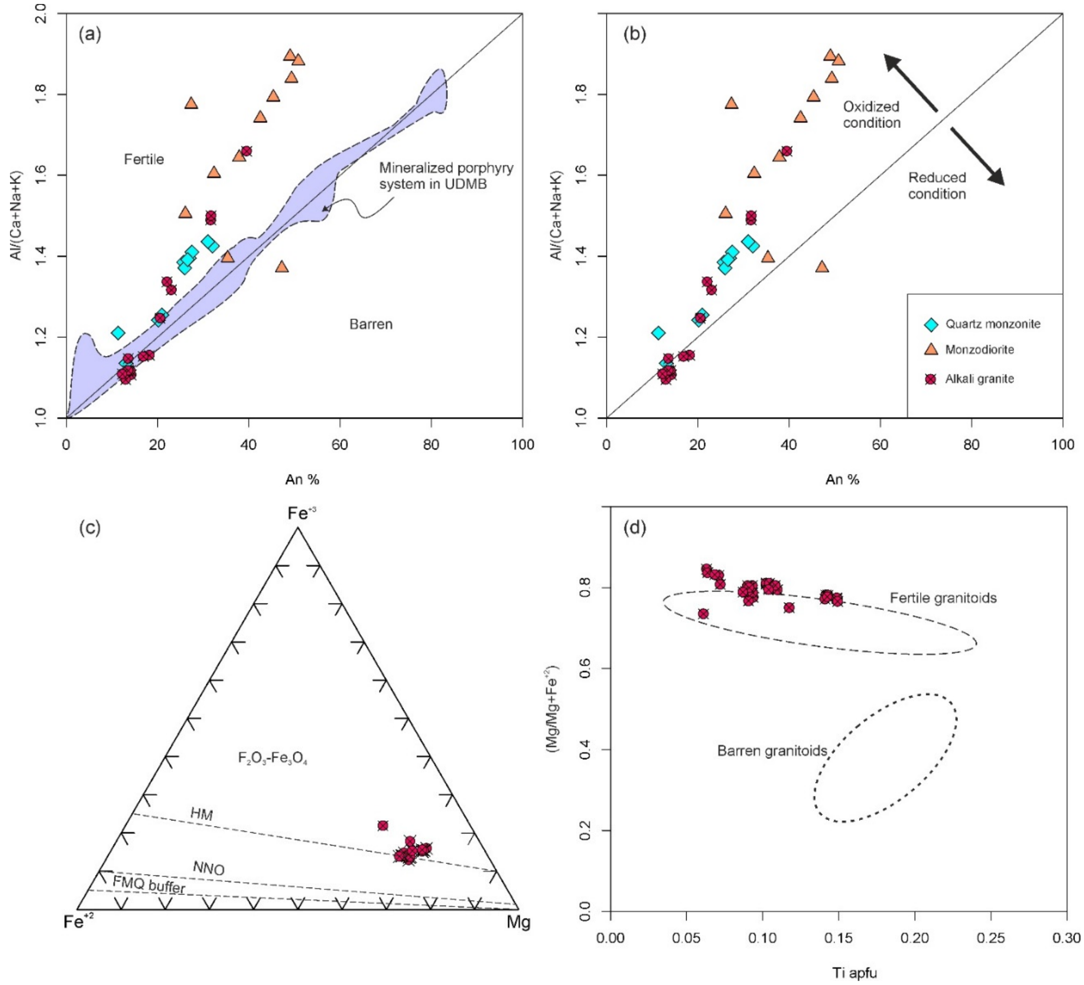

Figure 9. (a) The Al/(Ca+Na+K) versus anorthite contents diagram (after Williamson et al. 2016; Rezaei and Zarasvandi, 2022); (b) The Al/(Ca+Na+K) versus anorthite contents diagram to discriminate oxidized and reduced igneous rocks (Rezaei and Zarasvandi, 2022); (c) Fe^{+2}-Fe^{+3}-Mg ternary diagram (Wones and Eugster, 1965) for the alkali granite biotites to determine oxygen fugacity of the host magma; (d) Ti versus Mg# diagram to discriminate biotites from fertile and barren intrusions (after Taghavi et al., 2022)

Therefore, its composition could reflect geochemical characteristics of the hydrothermal fluid. The Fe^{+2}-Fe^{+3}-Mg ternary diagram (Wones and Eugster, 1965) indicates that the biotite formed in a high oxygen fugacity condition (Hematite-magnetite buffer) (Fig. 9c) that is suitable for a porphyry mineralization system (Richards et al., 2001; Asadi et al., 2014). The biotite chemical compositions also resemble those of the UDMB fertile granitoids (Fig. 9d).

Although, chemical compositions of the plagioclase and biotite of the quartz monzonite, quartz monzodiorite and alkali granite are consistent with fertile intrusive rocks, the presence of clinopyroxene and low amounts of biotite in the alkali granites demonstrate that their magma was relatively dry. Therefore, they could not cause vast porphyry type mineralization in the area.

Conclusion

According to petrographic studies, igneous rock of the NW Takestan area from the west AMB include monzodiorite, quartz monzonite, alkali granite, dacite, basalt and andesite together with pyroclastic units (tuff, agglomerate, and ignimbrite). The ocelli quartz, embayed, rounding and sieve-textured plagioclase, as well as the pyroxene phenocrysts surrounded by thin layers of second-generation fine pyroxenes in basaltic and basaltic andesitic samples are evidence for magmatic mixing/mingling in these rocks.

The clinopyroxenes from the basalts are augite and the others are diopside. The amphiboles are pargasite in the andesites. The biotites from the alkali granites have high phlogopite contents that were affected by hydrothermal fluids, while those from the andesites are primary, and contain lower phlogopite contents. The plagioclases have labradorite to andesine compositions in the basalts and andesine to oligoclase in the other rocks. They also have normal but relatively irregular chemical zoning profiles.

Geothermometry calculations based on the clinopyroxene, amphibole, plagioclase, orthoclase and biotites produced 880 to 980 °C for the basalt, 800 to 850 °C for the andesite and the dacite, 750 to 820 °C for the monzodiorites and the quartz monzonite, and 520 to 670 °C for the alkali granites.

Chemical compositions of the clinopyroxene, amphiboles and biotite indicate that the host magma was calc-alkaline formed during subduction of Neo-Tethys oceanic lithosphere beneath the central Iran microplate. That is in agreement with geotectonic theories represented using whole-rock geochemistry of the igneous rocks in other parts of the AMB and also confirms them for the western parts (Takestan area).

The plagioclase and biotite compositions of the monzodiorite, quartz monzonite, and alkali granite are consistent with fertile porphyry system intrusive rocks. They caused propylitic and argelic alterations probably at depth. This can be a subject of future explorations for Cu ± Au in the area.

Acknowledgment

We thank Prof. Lorence G. Collins for his editorial comments on the manuscript of this paper.

References

Abdel-Rahman, A., 1994. Nature of Biotite from Alkaline, Calc-alkaline, and Peraluminous Magmas. Journal of Petrology, 35: 525-41

Afshooni, S.Z., Mirnejad, H., Esmaeily, D., Haroni, H.A., 2013. Mineral chemistry of hydrothermal biotite from the Kahang porphyry copper deposit (NE Isfahan), Central Province of Iran. Ore Geology Reviews, 54: 214-232

Agard, P., Omrani, J., Jolivet, L., Whitechurch, H., Vrielynck, B., Spakman, W., Monié, P., Meyer, B., Wortel, R., 2011. Zagros orogeny: A subduction-dominated process. Geology Magazine, 148: 692 - 725

Aghazadeh, M., Castro, A., Badrzadeh, Z., Vogt, K., 2011. Post-collisional polycyclic plutonism from the Zagros hinterland: The Shaivar Dagh plutonic complex, Alborz belt, Iran. Geological Magazine, 148: 980-1008

Alai Mahabadi, S. Fanoudi, M., 1992. Geological Map of Takestan Quadrangle. Geological Survey of Iran. Scale 1:100000.

Amidi, S.M., Michel, R., 1985. Cenozoic magmatism of the Surk area (central Iran) stratigraphy, petrography, geochemistry and their geodynamic implications. Geologie Alpine, 61: 1-16

Amidi, S.M., Emami, M.H., Michel, R., 1984. Alkali character of Eocene volcanism in the middle part of central Iran and its geodynamic situation. Geologische Rundschau, 73: 917-932

Anderson, J.L., Smith, D.R., 1995. The effects of temperature and fO2 on the Al-in-hornblende barometer. American Mineralogist, 80: 549-59

Annells, R.N., Arthurton, R.S., Bazely, R.A., Davis, R.G., 1975. Explanatory text of the Qazvin and Rasht quadrangles map. Geological Survey of Iran. Scale 1:250000.

Ashrafi, N., Ahmad Jahangiri, A., Hasebec, N., Eby, G.N., 2019. Petrology, geochemistry and geodynamic setting of Eocene-Oligocene alkaline intrusions from the Alborz-Azerbaijan magmatic belt, NW Iran. Geochemistry, 78: 432-461

Asiabanha, A., Foden, J., 2012. Post-collisional transition from an extensional volcano-sedimentary basin to a continental arc in the Alborz Ranges, N-Iran. Lithos, 148: 98-111

Asiabanha, A., Bardintzeff, J.M., Kananian, A., Rahimi, G., 2012. Post-Eocene volcanics of the Abazar district, Qazvin, Iran: Mineralogical and geochemical evidence for a complex magmatic evolution. Journal of Asian Earth Sciences, 45: 79-94

Asiabanha, A., Ghasemi, H., Meshkin, M., 2009. Paleogene continental-arc type volcanism in North Qazvin, North Iran: facies analysis and geochemistry. Neues Jahrbuch für Mineralogie Abhandlungen, 186: 201-214

Avanzinelli, R., Bindi, L., Menchetti, S., Conticelli, S., 2004. Crystallization and genesis of peralkaline magmas from Pantelleria Volcano, Italy: an integrated petrological and crystal-chemical study. Lithos, 73: 41-69

Barrière, M., Cotton, J., 1979. Biotites and associated minerals as markers of magmatic fractionation and deuteric equilibration in granites. Contributions to Mineralogy and Petrology 70, 183-192

Beccaluva, L., Maccciotta, G., Piccardo, G.B., Zeda, O., 1989. Clinopyroxene composition of ophiolite basalts as petrogenetic indicator. Chemical Geology, 77: 165-182

Berberian, F., Berberian, M., 1981. Tectono-plutonic episodes in Iran. In: Gupta, H.K., Delany, F.M. (Eds.), Zagros Hindukush: Himalaya Geodynamic Evolution. American Geophysical Union, 5-32

Best, M.G., Christiansen, E.H., 2001. Igneous Petrology. Oxford Blackwell Science, 458 pp.

Bindi, L., Cellai, D., Melluso, L., Conticelli, S., Morra, V., Menchetti, S., 1999. Crystal chemistry of clinopyroxene from alkaline undersaturated rocks of the Monte Vulture Volcano, Italy. Lithos 46: 259-274

Blundy, J.D., Holland, T.J.B., 1990. Calcic amphibole equilibria and a new amphibole-plagioclase geothermometer. Contributions to Mineralogy and Petrolology 104: 208-24

Boomeri, M., Nakashima, K., Lentz, D.R., 2010. The Sarcheshmeh porphyry copper deposit, Kerman, Iran: a mineralogical analysis of the igneous rocks and alteration zones including halogen element systematics related to Cu mineralization processes. Ore Geology Reviews 38: 367-381

Castro, A., Aghazadeh, M., Badrzadeh, Z., Chichorro, M., 2013. Late Eocene-Oligocene post-collisional monzonitic intrusions from the Alborz magmatic belt, NW Iran. An example of monzonite magma generation from a metasomatized mantle source. Lithos 180-181: 109-127

Chiu, H.Y., Chung, S.L., Zarrinkoub, M.H., Mohammadi, S.S., Khatib, M.M., Iizuka, Y., 2013. Zircon U-Pb age constraints from Iran on the magmatic evolution related to Neotethyan subduction and Zagros orogeny. Lithos 162: 70-87

Danyushevsky, L.V., Sobolev, A.V., 1996. Ferric-ferrous ratio and oxygen fugacity calculations for primitive mantle-derived melts: calibration of an empirical technique. Mineralogy and Petrology 57: 229-2

Deer, W.A. Howie, R.A., Zussman, J., 1991. An introduction to the rock forming minerals. Longman Scientific Technical. 528 pp

Droop, G.T.R., 1987. A general equation for estimating Fe+3 concentrations in ferromagnesian silicates and oxides from microprobe analyses using stoichiometric criteria. Mineral Magazine 51: 431-435

Foudazi, M., Sheikhi Karizaki, H., Gholipuor, M., 2015. Petrology and geochemistry of granitoid massifs in North West of Takstan. Scientific Quarterly of Earth Sciences 24(95), 21-28 (in Persian with English abstract)

France, L., Koepke, J., Ildefonse, B., Cichy, S. B., Deschamps, F., 2010. Hydrous partial melting in the sheeted dike complex at fast spreading ridges: experimental and natural observations. Contributions to Mineralogy and Petrology 160: 683 -704.

Ghassemi, A., Dehnavi, R., Sarikhani, D., 2009. Geochemical and petrological characteristics of volcanic rocks of zajkan, north-west of Iran. Journal of the Indian Academy of Geoscience 52: 19-24

Guest, B., Horton, B.K., Axen, G.J., Hassanzadeh, J., McIntosh, W.C., 2007. Middle to late Cenozoic basin evolution in the western Alborz Mountains: Implications for the onset of collisional deformation in northern Iran. Tectonics 11: 1-26

Hammarstrom, J.M. Zen, E., 1986. Aluminum in hornblende: An empirical igneous geobarometer. American Mineralogist 71: 1297-313

Hawthorne, F.C., Oberti, R., Harlow, G.E., Maresch, W.V., Martin, R.F., Schumacher, J.C., Welch, M.D., 2012. Nomenclature of the amphibole supergroup. American Mineralogist 97: 2031-2048

Holland, T., Blundy, J., 1994. Non-ideal interactions in calcic amphiboles and their bearing on amphiboleplagioclase thermometry. Contributions to Mineralogy and Petrology 116: 433-47

Hollister, L.S., Grissom, G.C., Peters, E.K., Stowell, H.H., Sisson, V.B., 1987. Confirmation of the empirical correlation of Al in hornblende with pressure of solidification of calc-alkaline plutons. American Mineralogist 72: 231-9

Johnson, M.C., Rutherford, M.J., 1989. Experimental calibration of the aluminum-in-hornblende geobarometer with applicable to Long Valley Caldera (California) volcanic rocks. Geology 17: 837-41

Kazmin, V.G., Sbortshikov, I.M., Ricou, L.E., Zonenshain, L.P., Boulin, J., Knipper, A.L., 1986. Volcanic belts as markers of the Mesozoic-Cenozoic active margin of Eurasia. Tectonophysics 123: 123-152

Klein, C., Hurlbut, C. S., 1985. Manual of mineralogy. John Wiley and Sons, 596 pp.

Le Bas, M.J., 1962. The role of aluminum in igneous clinopyroxenes with relation to their parentage. American Journal of Science 260: 267-288

Leake, B.E., Woolley, A.R., Arps, C.E.S., Birch, W.D., Gilbert, M.C., Grice, J.D., Hawthorne, F.C., Kato, A., Kisch, H.J., Krivovichev, V.G., Linthout, K., Laird, J., Mandarino, J.A., Maresch, W.V., Nickel, E.H., Rock, N.M.S., Schumacher, J.C., Smith, D.C., Stephenson, N.C.N., Ungaretti, L., Whittaker, E.J.W., Guo, Y., 1997. Nomenclature of amphiboles; Report of the Subcommittee on Amphiboles of the International Mineralogical Association, Commission on New Minerals and Mineral Names. American Mineralogist 82: 1019-1037

Leterrier, J. Maury, R.C. Thonon, P. Girard, D., Marchal, M., 1982. Clinopyroxene composition as a method of identification of the magmatic affinities of paleo-volcanic series. Earth and Planetary Science. Letters 59: 139-154

Li, X., Chi, G., Zhou, Y., Deng, T., Zhang, J., 2017. Oxygen fugacity of Yanshanian granites in South China and implications for metallogeny. Ore Geology Reviews 88: 690-701

Madanipour, S., Ehlers, T.A., Yassaghi, A., Rezaeian, M., Enkelmann, E., Bahroudi, A., 2013. Synchronous deformation on the orogenic plateau margins, insights from the Arabia-Eurasia collision. Tectonophysics 608: 440-451

Manoli, S., Molin, G., 1988. Crystallographic procedures in the study of experimental rocks: X-ray singlecrystal structure refinement of clinopyroxene from Lunar 74275 high-pressure experimental basalt. Mineralogy and petrology 39: 187-200

Mohajjel, M., Fergusson, C., 2014. Jurassic to Cenozoic tectonics of the Zagros Orogen in northwestern Iran. International Geology Review 56: 263-287

Moin-Vaziri, H., 2004. An introduction to magmatism in Iran. Kharazmi University publication. 440 pp. (in Persian).

Molina, J., Scarrow, J., Montero, P.G., Bea, F., 2009. High-Ti amphibole as a petrogenetic indicator of magma chemistry: evidence for mildly alkalic-hybrid melts during evolution of Variscan basic-ultrabasic magmatism of central Iberia. Contribution to Mineralogy and Petrology 158: 69-98

Moromito, N., Fabrices J., Ferguson, A.K., Ginzburg, I.V., Ross, M., Seifer, F.A., Zussman, J., Akoi, K., Gottardi, G., 1988. Nomeclature of pyroxenes. Mineralogical Magazine 52: 535-550

Nabatian, G., Jiang, S., Honarmand, M., Neubauer, F., 2015. Zircon U-Pb ages, geochemical and Sr-Nd-Pb-Hf isotopic constraints on petrogenesis of the Tarom-Olya pluton, Alborz magmatic belt, NW Iran. Lithos 244: 43-58

Nachit, H., Abderrahmane, I., El Hassan, A., Mohcine, B.O., 2005. Discrimination between primary magmatic biotites, reequilibrated biotites and neoformed biotites. Geoscience 337: 1415-1420

Nisbet, E.G., Pearce, J.A., 1977. Clinopyroxene Composition in Mafic Lavas from Different Tectonic Settings. Contributions to Mineralogy and Petrology, 63: 149-160

Omrani, H., Michaeli, R., Moazzen, M., 2013. Geochemistry and petrogenesis of the Gasht peraluminous granite, western Alborz Mountains, Iran. Neues Jahrbuch für Geologie und Paläontologie, 268: 175-189

Pazirandeh, M., 1973. Distribution of volcanic rocks in Iran and a preliminary discussion of their relationship to tectonics. Bulletin Volcanologique, 37: 573-585

Putirka, K.D., 2008. Thermometers and Barometers for Volcanic Systems. Reviews in Mineralogical Society of American, 69: 61-120

Rezaei, M., Zarasvandi, A., 2022. Combined Feldspar-Destructive Processes and Hypogene Sulfide Mineralization in the Porphyry Copper Systems: Potentials for Geochemical Signals of Ore Discovering. Iranian Journal of Science and Technology 46: 1413-1424

Richards, J.P., Boyce, A.J., Pringle, M.S., 2001. Geological evolution of the Escondida area, northern Chile: a model for spatial and temporal localization of porphyry Cu mineralization. Economic Geology, 96: 271-305

Richards, J.P., 2016. Clues to hidden copper deposits. Nature Geoscience 9: 195-196.

Ridolfi, F., Renzulli, A., Puerini, M., 2009. Stability and chemical equilibrium of amphibole in calc-alkaline magmas: an overview, new thermobarometric formulations and application to subduction-related volcanoes. Contributions to Mineralogy and Petrology 160: 45-66

Ridolfi, F., Renzulli A., 2012. Calcic amphiboles in calc-alkaline and alkaline magmas: thermobarometric and chemometric emprical equations valid up to 1130 C and 2.2 Gpa. Mineralogy and Petrology, 163: 877-895

Rutter, M.J., Van der Laan S.R., Wyllie P.J., 1989. Experimental data for a proposed empirical igneous geobarometer: Aluminium in hornblende at 10 kbar pressure. Geology, 17: 897-900

Schmidt, M.W., 1992. Amphibole composition in tonalite as a function of pressure: An experimental calibration of the Al-in-hornblende barometer. Contributions to Mineralogy and Petrology, 110: 304-10

Schumacher, J.C., 2007. Metamorphic amphiboles: composition and coexistence. In: Hawthorne, F.C., Oberti, R., Della Ventura, G., Mottana, A. (Eds.), Amphiboles: crystal chemistry occurrence and health issues, reviews in mineralogy and geochemistry (67). Mineralogical Society of America, Washington, D.C, pp. 359-416

Selby, D., Nesbitt, B.E., 2000. Chemical composition of biotite from the Casino porphyry Cu-Au-Mo mineralization, Yukon, Canada: evaluation of magmatic and hydrothermal fluid chemistry. Chemical Geology, 171: 77-93

Shahabpour, J., 2007. Island-arc affinity of the Central Iranian Volcanic Belt. Journal of Asian Earth Sciences 30: 652-665

Siahcheshm, K., Calagari, A.A., Abedini, A., Lentz, D.R. 2012. Halogen signatures of biotites from the Maher-Abad porphyry copper deposit, Iran: characterization of volatiles in syn-to post-magmatic hydrothermal fuids. International Geology Reviews, 54: 1353-136

Stöcklin, J., 1974. Northern Iran: Alborz mountains. In: Spencer, A. (Ed.), Mesozoic-Cenozoic orogenic belts: data for orogenic studies. Geological Society Special Publication, pp. 213-234

Takin, M., 1972. Iranian geology and continental drift in the Middle East. Nature, 235: 147-150

Tang, P., Chen, Y., Tang, J., Wang, Y., Zheng, W., Leng, Q., Lin, B., Wu, E., 2019. Advances in research of mineral chemistry of magmatic and hydrothermal biotites. Acta Geologica Sinica, 93: 1947-1966

Van Lichtervelde, M., Grégoire, M., Linnen, R.L., Béziat, D., Salvi, S., 2008. Trace element geochemistry by laser ablation ICP-MS of micas associated with Ta mineralization in the Tanco pegmatite, Manitoba, Canada. Contribution to Mineralogy and Petrology, 155: 791-806

Verdel, C.S., Wernicke, B.P., Hassanzadeh, J., Guest, B., 2011. A Paleogene extensional arc flare-up in Iran. Tectonics, 30: 1-20

Vernon, R.H., 1991. Interpretation of Microstructures of Microgranitoid Enclaves. In: Didier, J., Barbarin, B. (Eds.), Enclaves and Granite Petrology 13. Elsevier, 277-292

Williamson, B.J., Herrington, R. J., Morris, A., 2016. Porphyry copper enrichment linked to excess aluminium in plagioclase. Nature Geoscience, 9: 237-241

Williamson, B.J., Hodgkinson, M., Imai, A., Takahashi, R., Armstrong, R.N., Herrington, R.J., 2018. Testing the Plagioclase Discriminator on the GEOROC Database to Identify Porphyry-Fertile Magmatic Systems in Japan. Resource Geology, 68(2): 138-143

Wones, D.R., Eugster, H.P., 1965. Stability of biotite: experiment, theory, and application. American Mineralogist, 50: 1228-1272

Yousefi, M., Omran, N.R., Lotfi, M., Bazoobandi, M.H., 2017. Copper and Gold Mineralization Features in Deh Bala Region-South of Takestan. Open Journal of Geology, 7: 1022-1046

Zanchi, A., Berra, F., Mattei, M., Ghassemi, M., Sabouri, J., 2006. Inversion tectonics in central Alborz, Iran. Journal of Structural Geology, 28: 2023-2037

Zarasvandi, A., Rezaei, M., Raith, J.G., Pourkaseb, H., Asadi, S., Saed, M., Lentz, D. R., 2018. Metal endowment reflected in chemical composition of silicates and sulfides of mineralized porphyry copper systems, Urumieh-Dokhtar magmatic arc, Iran. Geochimica et cosmochimica acta, 223: 36-59

Zhu, Y., Ogasawara, Y., 2004. Clinopyroxene phenocrysts (with green salite cores) in trachybasalts: implications for two magma chambers under the Kokchetav UHP massif, North Kazakhstan, Journal of Asian Earth Sciences, 22: 517-527